



Investigations on structural and optical properties of Al-modified ZnO nanoparticles

Shiv Kumar^{1,2} · Manish Kumar³ · Arvind Kumar³ · Subhash Sharma⁴ · Prashant Shahi⁵ · Sandip Chatterjee⁶ · Anup Kumar Ghosh²

Received: 15 February 2020 / Accepted: 24 March 2020 / Published online: 4 April 2020
© Springer Science+Business Media, LLC, part of Springer Nature 2020

Abstract

The current studies are concentrated on the synthesis of Al-modified ZnO nanoparticles prepared through sol–gel method for their structural and optical properties. The wurtzite structure with single phase formation for all the samples was confirmed from the Rietveld analysis on XRD data. Nano-crystalline nature (having particle size (~ 10 to 30 nm)) of all the synthesized samples have been examined by XRD and TEM data. Optical properties were carried out from UV–Vis, FTIR and Raman spectroscopy techniques. FTIR and Raman analysis also confirms the wurtzite structure and tetrahedral configuration with coordination of oxygen ions nearby the zinc ions. The UV–Vis measurement confirms that the bandgap is blue-shifted and slow red shift for lower and higher Al-concentrations in ZnO, respectively. Visible emission spectra of PL confirms the photo generated holes with deep-level emission, which is ascribed to recombination of electrons intensely spellbound in oxygen vacancies and zinc interstitials.

1 Introduction

There is a dynamic way of research in the current years through the doping in semiconducting nanoparticles as impurities can sturdily alter the structural, optical, electronic and magnetic properties [1, 2]. Such type of doped

semiconducting nanoparticles have turn out to be the foundation of numerous electronic and opto-electronic applications viz. diode junction rectifiers, photovoltaic solar cells, UV photodetectors, light emitters and also as transparent electrodes in thin-film devices [3–9]. After the addition of dopants for the duration of the developing route of nanostructures, they control the conditions of crystal development causing extreme changes in the morphology and inner defect creation [10, 11].

Among the various known semiconducting compounds, there is a well-known electro-optic and piezoelectric material, ZnO, have its place to II–VI group semiconductor. The nanoparticles of ZnO also have an optically transparent nature with hexagonal wurtzite structure having C_{6v}^4 ($P6_3mc$) space group and a wide direct bandgap of $E_g \sim 3.37$ eV with exciton-binding energy of ~ 60 meV. As per the theoretical studies, the ZnO nanoparticles have been recognized as a hopeful host material and have observed ferromagnetic nature above room temperature for the various transition metal-doped ZnO-based diluted magnetic semiconductors (DMSs) [12, 13]. It is also known as a suitable material for outstanding chemical, mechanical and thermal properties [14, 15].

Generally, ZnO is doped with Al, Ga or In for n-type [16–18] or P, N or Ar for p-type conductivity to enhance the properties of ZnO nanoparticles [19–21]. The Al-doped

✉ Manish Kumar
manishphy2007@gmail.com

✉ Arvind Kumar
arvindkumar@arsd.du.ac.in

¹ Hiroshima Synchrotron Radiation Center,
Hiroshima University, 2-313 Kagamiyama, Higashi,
Hiroshima 739-0046, Japan

² Materials Research Laboratory, Department of Physics,
Banaras Hindu University, Varanasi 221005, India

³ Experimental Research Laboratory, Department of Physics,
ARSD College, University of Delhi, New Delhi 110021,
India

⁴ CONACyT- Centro de Nanociencias y Nanotecnología,
Universidad Nacional Autónoma de México, Km 107
Carretera Tijuana-Ensenada s/n, C.P. 22800 Ensenada, B.C.,
Mexico

⁵ Department of Physics, Deen Dayal Upadhyaya Gorakhpur
University, Gorakhpur, Uttar Pradesh 273009, India

⁶ Department of Physics, IIT-BHU, Varanasi 221005, India

ZnO nanoparticles have gained immense attention as a transparent conducting oxide (TCO) for the device application in diverse optoelectronic devices mainly as flat-panel displays and transparent electrodes in the thin-film solar cells [22–25]. Nowadays, the frequently used TCO viz. fluorine-doped tin oxide (SnO₂:F) and tin-doped indium oxide (In₂O₃:Sn) are more costly and toxic as compared to the nontoxic Al-modified ZnO nanoparticles. On one side, the high demand and increased cost of indium is also the flaw in favour of it and gained the attention towards the low-cost materials recently [26]; on the other side, the opportunity of energy-efficient production methods of thin films by means of printing techniques of nano scaled precursors [27]. The Al-modified ZnO (AZO) nanoparticles are used as a transparent and conducting coating (top electrode) of solar cells and can also be used for the fabrication of polymer displays whereas located in a polyester medium [28].

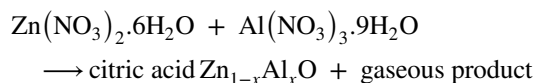
The studies confirmed that the replacement of Al³⁺-ions in place of Zn²⁺ ions causes additional point defects owing to the dissimilar ionic radii of Al³⁺ (~0.54 Å) and Zn²⁺ (~0.74 Å) ions [29]. Accumulation of small amount of Al-ions may be the reasons for quick alter of electronic properties. Recently, several studies [30–33] have been reported on Al-doped ZnO thin films to enhance its electronic and optical properties which are the basic prerequisite for its device application in optoelectronics. Lee et al. [34] also reported improved photo responsivity of UV sensors for Al-doped ZnO thin film structure. Masouleh et al. [35] studied Al-doped ZnO thin films for electrical and optical properties and found significant for plasmonic materials. In some recent studies by Shetti et al. [36–38], metal oxides (of ZnO and TiO₂) based nanostructures have also been studied in the realm of its uses in biomedical applications and found as a potential candidate for good sensing applications. ZnO along with other transition metal oxide (e.g. TiO₂, WO₃ and ZrO₂) is also known and used widely as photocatalysts for the hydrogen generation [39]. Other properties of Al-doped ZnO have also been explored by many research groups [40–45].

In the current investigations, we report on the synthesis of pure and Al-modified ZnO nanoparticles of the order of 10 nm size through the sol–gel method. Pure and Al-modified ZnO nanoparticles were characterized by the X-ray diffraction (XRD), transmission electron microscopy (TEM), Fourier transform-infrared spectroscopy (FTIR), UV–Vis absorption and Raman spectroscopy. The effect of Al-doping concentration in ZnO on the Photoluminescence and Raman scattering are also studied in detail.

2 Experimental details

Zn_{1-x}Al_xO (0 ≤ x ≤ 0.06) samples (named as Al-0, Al-0.5, Al-1, Al-2, Al-4 and Al-6 for Al-concentration x = 0, 0.005, 0.01, 0.02, 0.04 and 0.06 respectively) were prepared via the sol–gel route as followed by our group in previous study [46]. We have used high purity *Sigma-Aldrich chemicals* of zinc nitrate (Zn(NO₃)₂·6H₂O; purity 99.9%), aluminium nitrate (Al(NO₃)₃·9H₂O; purity 99.9%) and citric acid [C₆H₈O₇, 99.5%] as starting materials to synthesize the Al-modified ZnO nanoparticles. The calculated amount of required precursor in grams also tabulated in Table 1. In synthesis process, an appropriate amount of precursor, i.e. Zn(NO₃)₂·6H₂O and Al(NO₃)₃·9H₂O powders were taken, mixed and dissolved in 100 mL double distilled water to obtain a homogeneous solution. The mixture was then poured into citric acid [C₆H₈O₇] during the stirring. Citric acid serves as the fuel for the reaction. The precursor solution was further dried at 80 °C to obtain xerogel and the swelled xerogel was completed at 130 °C for 12 h to complete it. Final powder of Al-modified ZnO nanoparticles obtained after drying xerogel which was further ground and calcined at 600 °C for 10 h under air atmosphere.

The exothermic reaction can be articulated as follows:



The detail characterization techniques used to characterize the prepared samples in the present study have been discussed in our previous study [46].

3 Results and discussion

3.1 XRD study

Figure 1 shows the Rietveld refinement of the powder XRD patterns for Zn_{1-x}Al_xO (0 ≤ x ≤ 0.06) nanoparticles. XRD

Table 1 Amount (in grams) of different precursor used to synthesize Al-modified ZnO nanoparticles

Samples	Amount of Zn Precursor (g)	Amount of Al Precursor (gram)	Amount of citric acid (gram)
ZnO, Al-0	5.0	0.0	3.2290
Al-0.5	4.9685	0.0315	3.2245
Al-1	4.9371	0.0629	3.2194
Al-2	4.8746	0.1254	3.2150
Al-4	4.7504	0.2496	3.2018
Al-6	4.6275	0.3725	3.1878

data for ZnO and Al-doped ZnO nanoparticles (AZO) have been indexed with standard JCPDS (JCPDS 36–1451) data file. No secondary reflections have been observed even for the sample with maximum doping (6%) of Al. A detectable slight shift toward the higher angle side and broadening in the XRD peaks has been observed with increasing the Al-doping content (Fig. 1). This could be understood due to decrease in grain size and/or introduction of strain in ZnO lattice with the inclusion of Al-atoms. It is observed that the origin of strain in crystalline materials is due to stretching or compression between atomic bonds as a result of residual stress. It leads to changes in the spacing of crystallographic planes. As per the Bragg's law of diffraction, Bragg angles should either reduce or enhance while the spacing of the crystallographic plane changes. This results in shifting of XRD peaks towards lower and higher 2θ side as per the tensile stress with rising and compression stress, respectively. Hence, the tensile stress (therefore strain) has been developed due to the shifting of (101) peak of XRD towards lower 2θ in this system. To calculate the lattice parameters (a and c) for the samples, the following relation has been used [47]:

$$\sin^2 \theta = \frac{\lambda^2}{4} \left[\frac{4}{3} \left(\frac{h^2 + hk + k^2}{a^2} \right) + \frac{l^2}{c^2} \right] \quad (1)$$

where ' θ ' is the diffraction angle, λ is the incident wavelength (Cu-K α radiation) and h , k and l are Miller's indices.

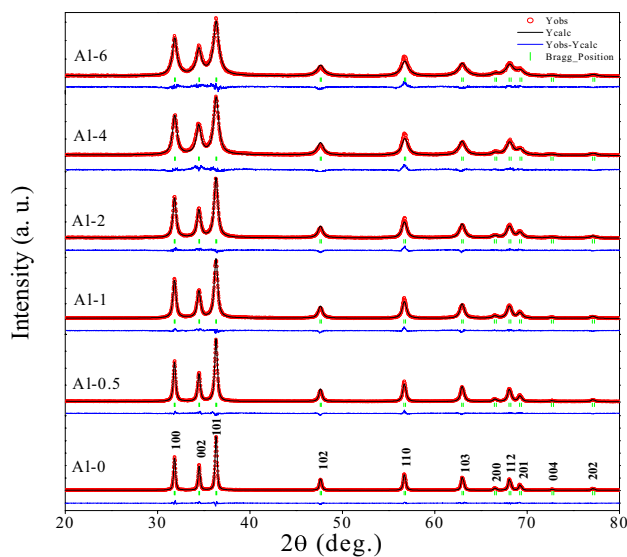


Fig. 1 Rietveld refinement profiles of powder XRD data for $\text{Zn}_{1-x}\text{Al}_x\text{O}$ ($0 \leq x \leq 0.06$) nanoparticles. The dots represent the observed data, whereas solid line through dots is the calculated profile, vertical ticks below curves represent allowed Bragg reflections for the wurtzite phase. The difference pattern is given below the vertical ticks

Crystallite size of ZnO and AZO nanoparticles has also been estimated using the well-known Scherrer's relation [48, 49]

$$D = \frac{0.9\lambda}{\beta \cos \theta} \quad (2)$$

where λ is the wavelength ($\lambda = 1.5406 \text{ \AA}$), θ is the Bragg diffraction angle and β is FWHM.

Figure 2a, b shows the variation of crystallite size calculated using Scherrer's relation and lattice strain with Al-concentration in ZnO nanoparticles, respectively. Crystallite size found to decrease with the increase of Al-concentration into ZnO nanoparticles (Fig. 2a) while the lattice strain found to increase with the increase of Al-concentration into ZnO nanoparticles (Fig. 2b). The calculated values of lattice parameters, inter planer spacing (d) and lattice volume (V) with the variation of Al-concentration (x) have shown in Fig. 3a–c, respectively. The atomic radius of Al^{3+} ($\sim 0.54 \text{ \AA}$) is less than the Zn^{2+} ($\sim 0.74 \text{ \AA}$) [29] which manifests as a reduction in the lattice parameters ' a ' and expansion in lattice parameter ' c '. An organized investigation of the d -spacing in (100), (002) and (101) planes have been done to be sentient of surface deformation caused by the doping in the system. The case of (100) plane shows the similar kind of actions like that of the lattice parameter ' a ' and for (002) and (101) planes, it follows the actions of lattice parameter ' c '. With the change in lattice parameter, lattice volume also changes. With increasing Al-concentration, the intensity of the diffraction peaks decreases and instantaneous increase in the FWHM. Such type of performance of the samples indicates that increment in doping concentration deteriorates the crystallinity, which possibly will be ascribed to the solidity stress arise due to the dissimilarity in the ionic radii of Al^{3+} ($\sim 0.54 \text{ \AA}$) and Zn^{2+} ($\sim 0.74 \text{ \AA}$) ions. This outcome can be with no trouble related with the alter in lattice parameters, due to lesser ionic radius of the Al-substituting Zn; therefore, causing minor distortions in the Al-doped ZnO lattice foremost to lesser particle sizes. The concentration of Zn interstitials is abridged for charge recompense in case of trivalent cation doping and as a resultant in concealed ZnO grain expansion and suggestive of the inclusion of Al into ZnO nanoparticles [50, 51].

3.2 TEM study

TEM images of the Al-1 sample have shown in Fig. 4. Particle size estimated from the TEM micrograph found to range from ~ 10 to 30 nm which are more or less spherical as shown in Fig. 4a. The average particle size of Al-1 samples obtained from TEM image matches well with the size calculated from the powder XRD data. The HRTEM images of a selected zone of the Al-1 sample are shown in Fig. 4b, c. The selected area electron diffraction (SAED) patterns

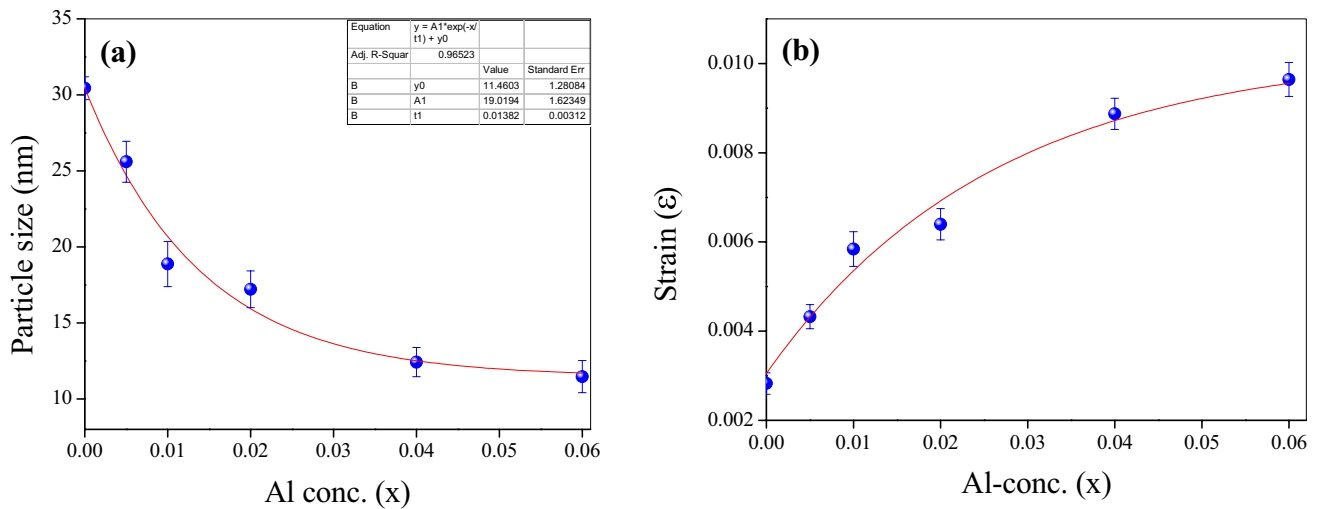


Fig. 2 Variation of (a) particle size (b) strain (ϵ) with Al-concentration (x) of the $Zn_{1-x}Al_xO$ nanoparticles

confirm the polycrystalline nature with the hexagonal-like shape of the prepared sample.

3.3 Raman spectroscopic study

Raman spectroscopy has been carried out for ZnO and AZO samples to explore the nature of crystallinity of the samples and influence of doping (disorder and defects in host lattice) into ZnO structure [49]. Figure 5 shows the Raman Spectra of ZnO and Al-modified ZnO, i.e., AZO nanoparticles. The present Raman study has been performed through micro-Raman spectroscopy, which is known to be a very delicate technique to identify local structural disorder created in the host lattice due to substitution of Al-ions into the ZnO nanoparticles prepared through sol–gel route [52].

Group theory predicts 12 phonon branches, in which nine of optical and three of acoustic for wurtzite phase of ZnO and at the centre (Γ) of the Brillouin zone, lattice optical phonons can be arranged as:

$$\Gamma = 1A_1 + 2B_1 + 1E_1 + 2E_2 \quad (3)$$

A_1 and E_1 modes in the above relation are known to be active for Raman and infrared spectroscopy. These modes are identified as polar and can be divided into transverse optical (TO) and longitudinal optical (LO) phonons. B_1 mode identified as inactive (silent) for both (infrared and Raman) spectroscopic technique. Two other nonpolar modes in the above relation, low frequency (E_2 mode) and high frequency (E_1 mode) found to be Raman active only.

Raman spectra shows the presence of all prominent peaks for both the ZnO and AZO nanoparticles. With the increment in Al percentage in the host ZnO sample, E_{2H}

mode becomes broad and found to be shifted at a higher frequency side. The intensity of E_{2H} mode found to be relatively less intense, whereas the intensity of $A_1(LO)$ mode found to increase. Such observations suggest that the crystal structure of doped sample (AZO) is the same as for undoped (ZnO) sample, but the local symmetry in the doped sample (AZO) is different from that of undoped (ZnO) sample. The peak observed at 434 cm^{-1} found to be sharpest and strongest and assigned as high-frequency E_2 mode (E_{2H}). The observed high-frequency mode involves the motion of oxygen which is characteristic of wurtzite structure and an indication of good crystallinity of the samples. For the 6% Al doping in the ZnO, E_{2H} mode shifts to 437 cm^{-1} . Significant broadening and weakening in nonpolar E_{2H} mode for the AZO samples have been found when compared with ZnO samples. This may be caused due to Al doping which results in the formation of lattice distortion and structural defect in doped ZnO (AZO) sample. The information about the stress-induced in the crystal can be extracted from the changes in E_2 phonon frequency. An increase/decrease in the E_2 phonon frequency is ascribed as compressive/tensile stress which is known to originate due to mismatch in the thermal expansion coefficients of the nanoparticles, lattice mismatch and distortion. Doping is considered to be the main cause of lattice distortion in the crystals since different elements have different atomic radii. In the present study, the nature of stress found to be compressive in synthesizing AZO nanoparticles. The difference mode between the E_2 high and E_2 low frequencies is assigned for the observed peak at nearby 330 cm^{-1} [53]. When comparing the Raman spectra of AZO with ZnO sample, it has been found that intensity of peak centred at $\sim 1050 \text{ cm}^{-1}$ and $\sim 1142 \text{ cm}^{-1}$ gradually increases and shifted slowly toward higher frequency side with increasing concentration of Al content in ZnO.

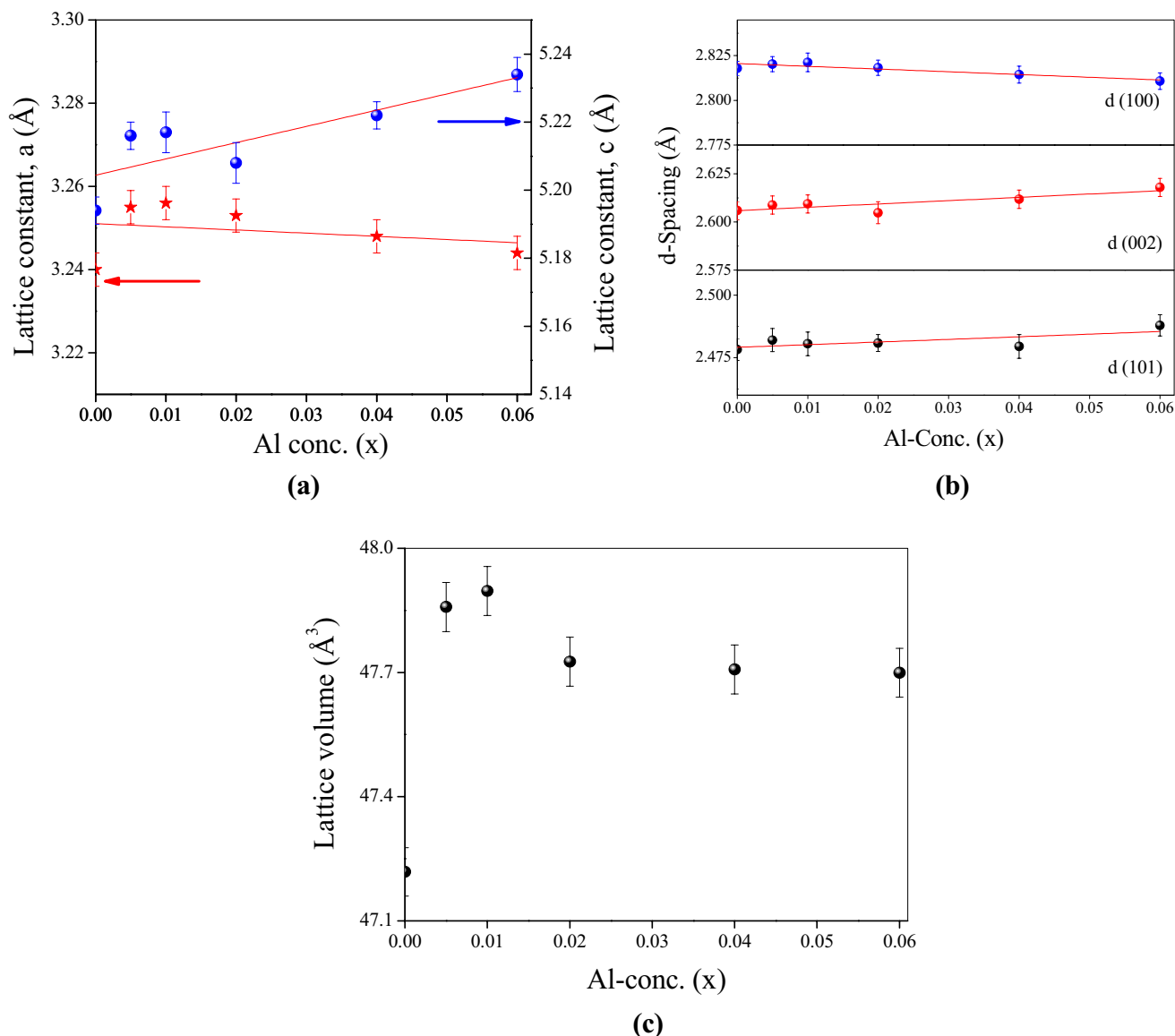


Fig. 3 **a** Variation of lattice parameter with Al-concentration (x) of the $Zn_{1-x}Al_xO$ nanoparticles. **b** Variation of the lattice spacing d_{101} , d_{002} and d_{100} three different planes for ZnO and AZO nanoparticles as

a function of dopant concentration. **c** Variation of lattice volume (V) with Al-concentration (x) of the $Zn_{1-x}Al_xO$ nanoparticles

3.4 FTIR spectroscopy study

The FTIR spectra in the wavenumber range $400\text{--}4000\text{ cm}^{-1}$ using KBr process for ZnO and AZO samples is shown in Fig. 6. FTIR technique has been used to collect the information of attached functional groups, molecular geometry and inter/intra-molecular interactions in the compound. We have observed a very prominent band at around 480 cm^{-1} and the negligibly weak band at around 668 cm^{-1} . These two bands are assigned to the stretching vibrations of

Zn–O in the tetrahedral and octahedral coordinations, respectively. The presence of these bands in the samples also confirm the formation of wurtzite phase of ZnO and AZO nanoparticles [54]. A strong asymmetric stretching mode of vibration has also been observed between the wavenumber ~ 1566 and 1547 cm^{-1} which is identified due to of C=O bond. Band arises at $\sim 2345\text{ cm}^{-1}$ may be due to the absorption of atmospheric CO_2 on the metallic cations. Another observed absorption peak at $\sim 3440\text{ cm}^{-1}$ for ZnO and AZO nanoparticles was assigned due to stretching and bending vibration of surface –OH groups.

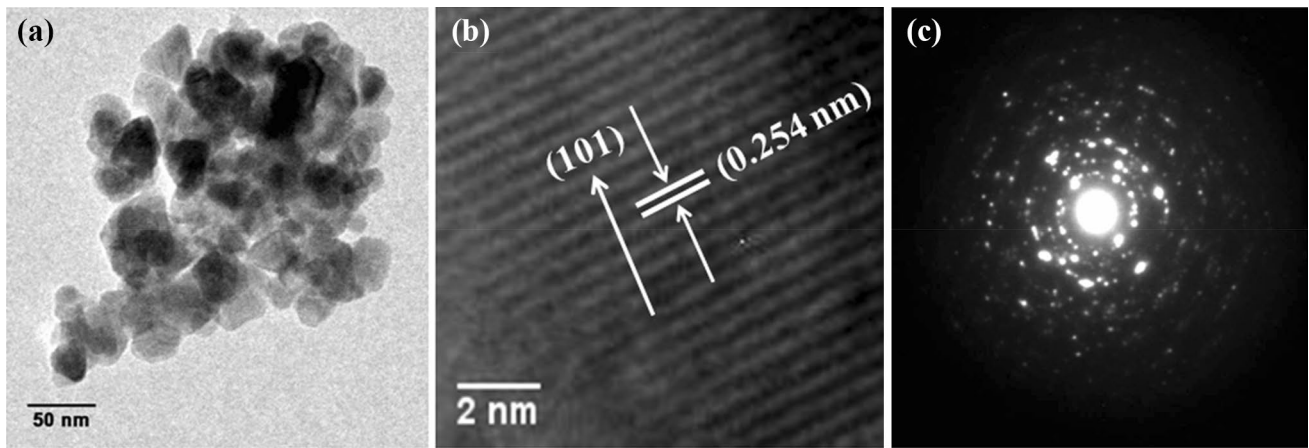


Fig. 4 TEM images of $Zn_{0.99}Al_{0.01}O$ nanocrystal: **a** at 50 nm resolution, **b** HRTEM and **c** SAED

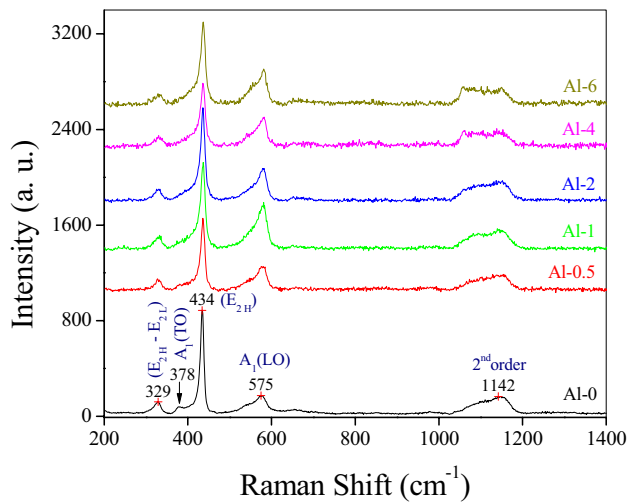


Fig. 5 Room-temperature micro-Raman spectra of $Zn_{1-x}Al_xO$ nanoparticles

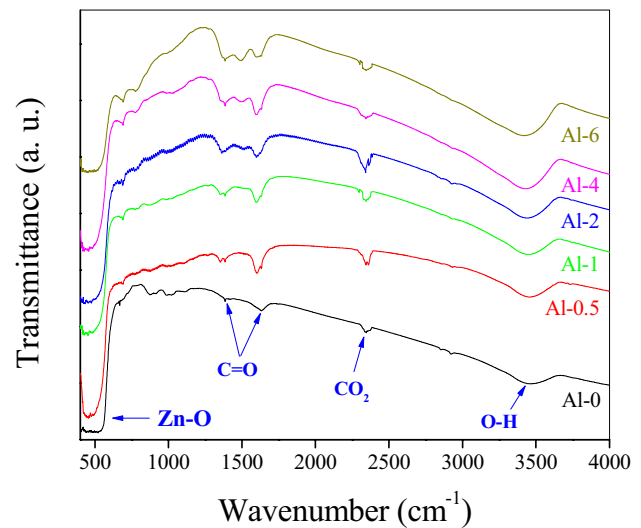


Fig. 6 FTIR spectra of $Zn_{1-x}Al_xO$ ($0 \leq x \leq 0.06$) nanoparticles

3.5 UV-Vis spectroscopy study

Doping of metals (like Al, Mg, Mn, etc.) in the semiconducting material causes some change in their bandgap. Changing the bandgap can have a strong effect on the optical properties of the material. UV-visible spectroscopy is a nondestructive technique to estimate the optical bandgap of the semiconducting material. The UV-visible spectra of the samples (in the range of 300–700 nm) have shown in Fig. 7. Strong absorption has been observed between 300 and 400 nm with sharp decrease afterwards. Absorption peak at around ~ 379 nm for ZnO nanoparticles shows the bandgap of 3.27 eV.

The optical band gap (E_g) was estimated using the Tauc's equation [55], $(ah\nu)^2 = A(h\nu - E_g)$ where E_g is the optical

band gap, A is a proportionality constant, $h\nu$ is the energy of the incident photon and α is the absorption coefficient.

Inset of Fig. 7 shows the variation of the optical band-gap of ZnO nanoparticles with Al-concentration and found to increase when compared with ZnO nanoparticles. The optical band gap was found to be increased from 3.27 to 3.33 eV with the increase of doping concentration up to 2% Al (inset of Fig. 7). The obtained increasing nature of the optical bandgap for Al-modified ZnO nanoparticles when compared with the ZnO nanoparticles could be attributed to the smaller particle size of AZO nanoparticles (as shown in Fig. 2a) For the higher concentration of Al, i.e. for 4% and 6% Al-concentration, optical bandgap was estimated 3.31 eV and 3.32 eV, respectively. Overall, the optical bandgap of ZnO found to vary between 3.27 and 3.33 eV depending on the size of nanoparticles. From the Fig. 7a, it has been clear

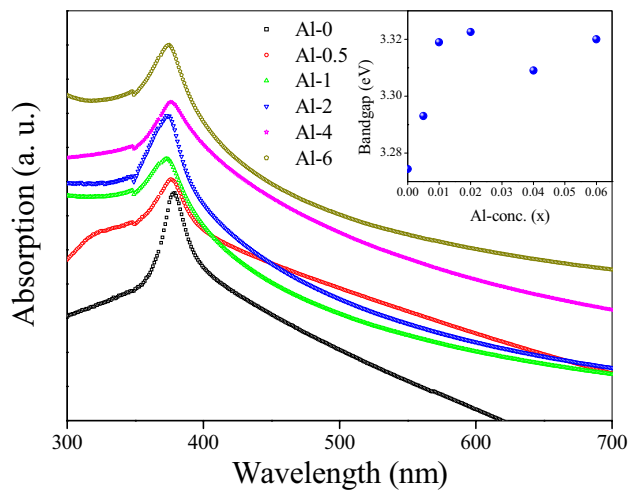


Fig. 7 Absorption spectra of $\text{Zn}_{1-x}\text{Al}_x\text{O}$ nanoparticles. Inset shows the variation of the optical band gap (E_g) with the Al-concentration (x)

that the bandgap is blue-shifted for lower concentration (up to 2% of Al) and shows red-shifted for higher concentration. The behaviour of variation in band gap is very much similar to the variation in unit cell volume of the doped nanoparticles.

It is well known that as the particle size decreases, the separation between conduction band and valence band energy levels gets increase due to the quantum confinement effect which results in a large bandgap [56, 57]. Similar behaviour of bandgap variation with the introduction of Al in the ZnO matrix, i.e. AZO nanoparticles has also been found by other research groups [57, 58]. Viswanatha et al. [59] also developed a realistic and accurate tight-binding (TB) approach to explain the blue-shift and correlate the absorption edge with the size of the nanocrystals. Our study also shows that the variation of optical band gap for Al-doped ZnO was not monotonic with dopant concentration and such observed behaviour was quite similar to that of the Al-doped ZnO thin film reported by Park et al. [60].

Thus, the increase in optical bandgap for AZO when compared with ZnO can be understood in terms of change in lattice constant. It is also may be due to formation of new states by the introduction of Al doping.

3.6 Photoluminescence spectroscopy study

The photoluminescence (PL) spectra of ZnO and AZO nanoparticles are shown in Fig. 8. The nanoparticles of ZnO and AZO have been excited with a wavelength of 320 nm at room temperature. Usually, the PL spectra of ZnO have two emission bands, one in the UV region and other in the visible region. PL spectra in UV region are due to the near-band-edge emission through exciton–exciton collision processes. Other visible region PL spectra may be attributed

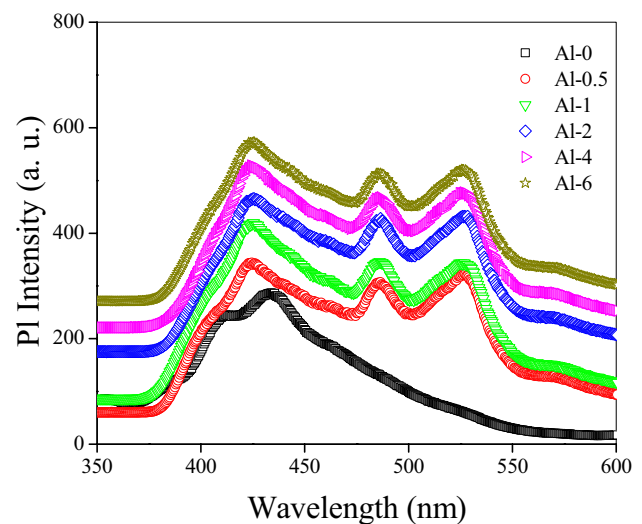


Fig. 8 Room temperature PL spectra of the $\text{Zn}_{1-x}\text{Al}_x\text{O}$ ($0 \leq x \leq 0.06$) nanoparticles

due to electron–hole recombination at a deep level emission in the bandgap which is due to intrinsic point defects, such as oxygen vacancies, zinc interstitials and photogenerated holes [61, 62].

As in present study, PL measurements have been performed with an excitation wavelength of 325 nm so the characteristic near-band-edge (NBE) emission of ZnO around 365 nm (~ 3.37 eV) in the UV region has not been recorded. PL spectra shows main broad emission peaks in the visible region for ZnO and AZO nanoparticles. As it can be seen from the PL spectra of AZO nanoparticles that in the visible region between 400 and 560 nm, broad peaks ~ 424 nm, 485 nm and 527 nm has been observed when compared with ZnO nanoparticles which shows a broad peak around ~ 434 nm. PL spectra of AZO samples show that visible deep level emission intensity increased with Al-concentration which is often due to the oxygen vacancies in different charge states and zinc interstitials.

4 Conclusions

Pure and Al-modified ZnO nanoparticles have been effectively prepared by sol–gel route. Rietveld refinement of XRD pattern confirms the formation of single-phase having wurtzite structure of ZnO and Al-doped ZnO nanoparticles. XRD and TEM measurements show the nanocrystalline nature of Al-doped ZnO with particle size range from ~ 10 to 30 nm. Raman spectroscopy measurements confirm the similar crystal structure, i.e. wurtzite in pure and Al modifies ZnO samples, even the confined symmetry in the doped samples is dissimilar from that of pure ZnO sample. FTIR spectra also confirms the wurtzite structure and arrangement of

tetrahedral coordination of the oxygen ions nearby the zinc ions. The bandgap is blue-shifted in lower Al-concentration and a slow red shift is observed in higher Al-concentration, which is confirmed from the UV–Vis spectra. Visible emission spectra of PL confirms the deep-level production and accredited to recombination of electrons intensely trapped in oxygen vacancies and zinc interstitials with photogenerated holes. Therefore, the present work deals with the detailed study on structural and optical properties of Al-modified ZnO nanoparticles. These materials could be used effectively in different optoelectronic devices and industrial applications, such as luminescent materials for fluorescent tubes, as an active medium for lasers and sensors, etc.

Acknowledgments The authors are thankful to UGC-DAE Indore and IUAC, New Delhi, for their experimental facilities. S. K. acknowledges the financial support from overseas postdoctoral fellowship, SERB-India (OPDF Award No.: SB/OS/OPDF-060/2015–16) and Prof. K. Shimada (Hiroshima Synchrotron Radiation Center, Hiroshima University, Japan).

References

- J.D. Bryan, D.R. Gamelin, *Progress in Inorganic Chemistry*, vol. 54 (Wiley, New York, 2005), p. 47
- D.J. Norris, A.L. Efros, S.C. Erwin, *Science* **319**, 1776 (2008)
- S. Coe, W.K. Woo, M. Bawendi, V. Bulovic, *Nature* **420**, 800 (2002)
- H.S. Yang, P.H. Holloway, B.B. Ratna, *J. Appl. Phys.* **93**, 586 (2003)
- K. Mohanta, S.K. Batabyal, A.J. Pal, *Chem. Mater.* **19**, 3662 (2007)
- D.C. Olson, Y.J. Lee, M.S. White, N. Kopidakis, S.E. Shaheen, D.S. Ginley, J.A. Voigt, J.W.P. Hsu, *J. Phys. Chem. C* **111**, 16640 (2007)
- Y.Z. Jin, J.P. Wang, B.Q. Sun, J.C. Blakesley, N.C. Greenham, *Nano Lett.* **8**, 1649 (2008)
- V. Mahalingam, V. Sudarsan, P. Munusamy, F. van Veggel, R. Wang, A.J. Steckl, M. Raudsepp, *Small* **4**, 105 (2008)
- B.N. Pawar, G. Cai, D. Ham, R.S. Mane, T. Ganesh, A. Ghule, R. Sharma, K.D. Jadhava, S.H. Han, *Sol. Energy Mater. Sol. Cells* **93**, 524 (2009)
- J.U. Brehm, M. Winterer, H. Hahn, *J. Appl. Phys.* **100**, 064311 (2006)
- Y. Liu, J. Lian, *Appl. Surf. Sci.* **253**, 3727 (2007)
- T. Dietl, H. Ohno, F. Matsukura, J. Cibert, D. Ferrand, *Science* **287**, 1019 (2000)
- K. Sato, H. Katayama-Yoshida, *Jpn. J. Appl. Phys.* **39**, L555 (2000)
- Z.L. Wang, *J. Phys.* **16**, R829–R858 (2004)
- R. Suntako, *IOP Conf. Ser.* **284**, 012017 (2017)
- H. Agura, A. Suzuki, T. Matsushita, T. Aoki, M. Okuda, *Thin Solid Films* **445**, 263 (2003)
- Z.F. Liu, F.K. Shan, Y.X. Li, B.C. Shin, Y.S. Yu, *J. Cryst. Growth* **259**, 130 (2003)
- M. Ahmad, J. Zhao, J. Iqbal, W. Miao, L. Xie, R. Mo, J. Zhu, *J. Phys. D* **42**, 165406 (2009)
- A. Allenic, W. Guo, Y.B. Chen, Y. Che, Z.D. Hu, B. Liu, X.Q. Pan, *J. Phys. D* **41**, 025103 (2008)
- S. Chakrabarti, B. Doggett, R. O’Haire, E. McGlynn, M.O. Henry, A. Meaney, J.P. Mosnier, *Superlattice Microstruct.* **42**, 21 (2007)
- H.-K. Choi, J.-H. Park, S.-H. Jeong, B.-T. Lee, *Semicond. Sci. Technol.* **24**, 105003 (2009)
- K.L. Chopra, S. Major, D.K. Pandya, *Thin Solid Films* **102**, 1 (1983)
- T. Minami, H. Nanto, S. Takata, *Jpn. J. Appl. Phys.* **23**, L280 (1984)
- K. Ellmer, A. Klein, B. Rech, *Transparent Conductive Zinc Oxide* (Springer Series in Material Science, Berlin, 2008), p. 104
- U. Ozgur, Y.I. Alivov, C. Liu, A. Teke, M.A. Reshchikov, S. Dogan, V. Avrutin, S.-J. Cho, H. Morkoc, *J. Appl. Phys.* **98**, 041301 (2005)
- T.D. Kelly, G.R. Matos, in *Historical Statistics for Mineral and Material Commodities in the United States* (2011)
- C.G. Granqvist, *Sol. Energy Mater. Sol. Cells* **91**, 1529 (2007)
- E. Fortunato, P. Nunes, D. Costa, D. Brida, I. Ferreira, R. Martins, *Vacuum* **64**, 233 (2002)
- C. Klingshirn, *Phys. Status Solidi B* **244**, 3027 (2007)
- K.N. Tonny, R. Rafique, A. Sharmin, M.S. Bashar, Z.H. Mahmood, *AIP Adv.* **8**, 065307 (2018)
- H. Zheng, R.J. Zhang, D.-H. Li, X. Chen, S.Y. Wang, Y.X. Zheng, M.J. Li, Z.G. Hu, N. Dai, L.Y. Chen, *Nanoscale Res. Lett.* **13**, 149 (2018)
- N. Krstulovic, K. Salamon, O. Budimilija, J. Kovac, J. Dasovic, P. Umek, I. Capan, *Appl. Surface Sci.* **440**, 916 (2018)
- P. Swapna, S.V. Reddy, *Asian J. Nanosci. Mater.* **2**, 111 (2018)
- W. Lee, J.Y. Leem, *J. Korean Phys. Soc.* **72**, 610 (2018)
- F.F. Masouleh, I. Sinno, R.G. Buckley, G. Gouws, C.P. Moore, *Appl. Phys. A* **124**, 174 (2018)
- N.P. Shetti, S.D. Bukkitgar, K.R. Reddy, C.V. Reddy, T.M. Aminabhavi, *Biosens. Bioelectron.* **141**, 111417 (2019)
- N.P. Shetti, S.D. Bukkitgar, K.R. Reddy, C.V. Reddy, T.M. Aminabhavi, *Colloids Surfaces B* **178**, 385–394 (2019)
- N.P. Shettia, S.J. Malodea, D.S. Nayaka, G.B. Bagihallia, S.S. Kalanurb, R.S. Malladic, C. Reddyd, T.M. Aminabhavie, K.R. Reddy, *Appl. Surface Sci.* **496**, 143656 (2019)
- S.B. Patil, P.S. Basavarajappa, N. Ganganagappa, M.S. Jyothi, A.V. Raghu, K.R. Reddy, *Int. J. Hydrog. Energy* **4**(4), 13022–13039 (2019)
- A. Djelloul, Y. Larbah, M. Adnane, B. Labdelli, M.I. Ziane, A. Manseri, A. Messaoud, *J. Nano- Electron. Phys.* **10**, 02036 (2018)
- J.T. Luo, A.J. Quan, Z.H. Zheng, G.X. Liang, F. Li, A.H. Zhong, H. Li, X.H. Zhang, P. Fan, *RSC Adv.* **8**, 6063 (2018)
- X.Q. Gu, L.P. Zhu, L. Cao, Z.Z. Ye, H.P. He, P.K. Chu, *Mater. Sci. in Semicon. Process* **14**, 48 (2011)
- P. Cao, Y. Bai, D.X. Zhao, D.Z. Shen, *Mater. Sci. in Semicon. Process.* **14**, 73 (2011)
- K.M. Sandeep, S. Bhat, S.M. Dharmaprakash, *Mater. Sci. in Semicon. Process.* **56**, 265 (2016)
- B.K. Shin, T.I. Lee, J.P. Kar, M.J. Lee, K.I. Park, K.J. Ahn, K.Y. Yeom, J.H. Cho, J.M. Myoung, *Mater. Sci. Semicon. Process.* **14**, 23 (2011)
- S. Kumar, S. Mukherjee, R.K. Singh, S. Chatterjee, A.K. Ghosh, *J. Appl. Phys.* **110**, 103508 (2011)
- B.D. Cullity, *Elements of X-Ray Diffractions* (Addison-Wesley, Reading, MA, 1978)
- A.L. Patterson, *Phys. Rev.* **56**, 972 (1939)
- J.B. Wang, G.J. Huang, X.L. Zhong, L.Z. Sun, Y.C. Zhou, E.H. Liu, *Appl. Phys. Lett.* **88**, 252502 (2006)
- S. Fujihara, A. Suzuki, T. Kimura, *J. Appl. Phys.* **94**, 2411 (2003)
- M. Wang, K.E. Lee, S.H. Hahn, E.J. Kim, S. Kim, J.S. Chung, E.W. Shin, C. Park, *Mater. Lett.* **61**, 1118 (2007)
- A. Singhal, S.N. Achary, J. Manjanna, S. Chatterjee, P. Ayyub, A.K. Tyagi, *J. Phys. Chem. C* **114**, 3422 (2010)
- R. Cusco, E. Alarcon-Llado, J. Ibanez, L. Artus, *Phys. Rev. B* **75**, 165202 (2007)

54. R. Elilarassi, G. Chandrasekaran, *Mat. Chem. Phys.* **123**, 450 (2010)
55. V. Kumar, S. Sharma, T.P. Sharma, V. Singh, *Opt. Mater.* **12**, 115 (1999)
56. M.R. Islam, J. Podder, M.M. Islam, R.I. Chowdhury, S.F.U. Farhad, D.K. Saha, *Sens. Transducers* **134**, 170 (2011)
57. K. Lin, H. Cheng, H. Hsu, L. Lin, W. Hsieh, *Chem. Phys. Lett.* **409**, 208 (2005)
58. Y. Zhang, Y. Yang, J. Zhao, R. Tan, W. Wang, P. Cui, W. Song, *J. Mater. Sci.* **46**, 774–780 (2011)
59. R. Viswanatha, S. Sapra, B. Satpati, P.V. Satyam, B.N. Dev, D.D. Sarma, *J. Mater. Chem.* **14**, 661 (2004). <https://doi.org/10.1039/b310404d>
60. R.P. Wang, A.W. Sleight, *Chem Mater* **8**, 433 (1996)
61. A.V. Dijken, E.A. Meulenkamp, D. Vanmaekelbergh, A. Meijerink, *J. Lumin.* **90**, 123 (2000)
62. D. Raoufi, *J. Luminescence* **134**, 213 (2013)

Publisher's Note Springer Nature remains neutral with regard to jurisdictional claims in published maps and institutional affiliations.